IEEE Access
Multidisciplinary | Rapid Review | Open Access Journal

Received 7 November 2024, accepted 23 November 2024, date of publication 2 December 2024, date of current version 10 December 2024.

*Digital Object Identifier 10.1109/ACCESS.2024.3509640*

RESEARCH ARTICLE

# LUNA: Loss-Construct Unsupervised Network Adjustment for Low-Dose CT Image Reconstruction

**RITU GOTHWAL, SHAILENDRA TIWARI, AND SHIVENDRA SHIVANI**
Thapar Institute of Engineering and Technology, Patiala 147004, India
Corresponding author: Ritu Gothwal (rgothwal60_phd18@thapar.edu)

**ABSTRACT** Reconstructing low-dose CT imaging deals with handling the inherent noise within the data, which makes it a complex mathematical problem known as an ill-posed inverse problem. Recent attention has shifted towards deep learning-based techniques in CT image reconstruction. However, these approaches encounter limitations due to extensive data requirements for training and validation. We propose an unsupervised CT reconstruction technique that leverages the power of Deep convolutional neural networks (Deep CNNs), demonstrating that a randomly initialized neural network can serve as a prior. We have proposed a completely unsupervised deep learning technique called Loss-construct unsupervised network (LUNA) adjustment for low-dose CT image reconstruction. Our approach combines the traditional reconstruction technique, i.e., simultaneous algebraic reconstruction technique (SART), and integrates the image prior i.e., weighted total variation (WTV) regularization within the Deep CNN model. The overall reconstruction process is optimized using the alternating direction method of multipliers (ADMM) framework, that balances the neural network's internal representation with the observed data, yielding a more consistent and accurate final image. The proposed method uses various loss functions to update the Deep CNN. The optimal update of the network depends on the various loss functions. Different loss functions, including perceptual loss, SSIM loss, WL2 loss, WTV loss, and sinogram loss, are used to guide the overall reconstruction. This approach effectively handles the constraints of data limitation of deep learning-based techniques, offering a robust and unsupervised solution for low-dose CT image reconstruction.

**INDEX TERMS** Low dose CT, unsupervised learning, SART, ADMM based optimization, loss functions.

## I. INTRODUCTION

Compute tomography (CT) [1] imaging serves as a diagnostic tool providing valuable clinical insights into the anatomical structures of the body, encompassing organs, tissues, bones, and blood arteries. The mathematical formulation of the CT reconstruction process is given as

$$D = \mathbf{A}e^* + \eta \tag{1}$$

The system matrix is denoted by $\mathbf{A}$. The vector $e^* \in R^p$, represents the unknown image in vector form and $\eta$ denotes the noise component. $D \in R^q$, represents the measurement vector corrupted by noise. Due to the significant disparity between the number of measurements, denoted as $q$, and the number of unknowns $p$, this particular scenario may be classified as a very under-determined linear inverse problem.

Nevertheless, prolonged exposure to X-ray radiation can lead to adverse consequences, such as an elevated risk of cancer, genetic issues, and other health conditions [2]. In response to this concern, low-dose computed tomography (LDCT) imaging protocols have been established by adjusting various settings on CT devices, such as tube current (mA) and tube potential (kVp), in alignment with the ALARA [3] radiation safety principle. However, modifying these device settings in LDCT procedures significantly affects the visual quality of the resulting LDCT images. Consequently, the acquired LDCT images may exhibit various artifacts and degradation, including quantum noise.

The associate editor coordinating the review of this manuscript and approving it for publication was Yi Zhang.

Various approaches aimed at enhancing the diagnostic quality of low-dose CT scan can be classified into sinogram refining [4], iterative reconstruction [5], and techniques based on deep learning [6].

Sinogram filtering [7], [8] is a procedure that involves applying a smoothing technique directly to the raw data before executing any reconstruction algorithm. Some of the techniques in this category are structural adaptive filtering [9], non-linear sinogram smoothing [10], bilateral filtering [11] and Penalized weighted least-squares (PWLS) [12].

Iterative reconstruction (IR) presents an alternative method for LDCT. Iterative reconstruction techniques make use of prior information in the reconstruction phase. For example Anisotropic diffusion (AD) [13], Nonlocal means (NLM) [14], Dictionary acquisition [15], low-rank matrix decomposition [16], techniques based on Statistical Models and Bayesian Inference [17]. Despite their effectiveness, iterative reconstruction techniques have a substantial processing cost.

Deep learning (DL) [18], [19], [20], [21] holds significant potential in advancing efficient image reconstruction algorithms for CT reconstruction, particularly in the context of LDCT [22]. The most of deep learning based techniques are based upon supervised learning [23].

Supervised learning methods typically require large datasets containing pairs of low-dose and corresponding normal-dose images, which are often complex and expensive to acquire. These datasets involve performing two scans per patient (one low dose and one regular dose) and ensuring the precise alignment of these images. This process is both costly and time-consuming. This endeavor is further complicated by variations in patient anatomy, imaging protocols, and scanner types, necessitating attention to distinct artifacts and noise patterns. Additionally, the availability of large, clean, and labeled datasets is limited, particularly in the case of low-dose CT (LDCT), where ethical concerns and the need to minimize radiation exposure restrict data collection. Furthermore, supervised approaches require significant manual effort from domain experts, such as radiologists, to annotate and evaluate the datasets. Creating reliable training data for supervised learning in medical imaging makes it even more challenging. Given these constraints, unsupervised deep learning methods have emerged as a powerful alternative, especially in data-limited environments. These methods do not rely on paired ground-truth images but instead learn from the data, and the Deep network itself can act as a regularizer within the reconstruction process. Unsupervised techniques allow models to generalize better across various data types and reduce the need for large-scale, labeled datasets, enabling broader applications in real-world scenarios where data collection is inherently limited.

This research presents an unsupervised technique for reconstructing LDCT images using a Deep Convolutional Neural Network (CNN). Deep image priors enable the network to acquire appropriate regularization directly from the data, which may result in enhanced reconstruction quality. The proposed technique LUNA operates independently of training and testing data. It employs (SART) as the reconstruction algorithm, utilizing the architecture of untrained deep neural networks as image priors. This design eliminates the necessity for external datasets or training examples. The main contribution of the proposed approach are

- We propose an unsupervised CT reconstruction technique that harnesses the capabilities of Deep CNNs, demonstrating that a randomly initialized neural network can function as a prior.
- The overall network performance depends upon the network updation done using various loss functions, including sinogram loss, perceptual loss, TV loss, SSIM loss, and L2 loss.
- ADMM is used to optimize the reconstruction process and balance out the NN internal representation with the observed data.

## II. RELATED WORK

Deep learning (DL) has been a popular technology in recent years for creating effective image reconstruction techniques in LDCT imaging. There are various deep learning networks which includes CNN [24], Convolutional auto-encoder [25], [26], [27], U-net [28], [29] that can be utilized in image reconstruction tasks. The reconstruction domain makes use of deep learning based approaches including, post-processing methods [19], [30], prepossessing [20], [31], [32], unrolling strategy [33] and plug-and-play [34], [35].

In post-processing setup Deep learning networks are used as a priors. The purpose of post-processing approaches is to improve the quality of applied reconstruction algorithms. Wolterink et al. [36] introduced a post-processing methodology that aims to predict regular-dose CT images by using low-dose CT images. Chen et al. [30] proposed a post-processing method known as RED-CNN for low-dose CT imaging based on auto-encoder. Yang et al. [19] suggested a post-processing-based deep learning approach that employs 2-D and 3-D residual convolutional networks.

There are deep-learning based approaches that can be effectively be used in sinogram domain or prepossessing. The investigation done by Bai et al. [37] developed a novel methodology that employs a deep learning model for the purpose of predicting the absent elements of a signal that weren't collected during the data collection phase. The filtered back projection (FBP) method is used to rebuild CT images after first making predictions based on the inadequate data. In the research [31] Deep Learning-enabled Iterative Reconstruction (Deep IR) strategy for CT denoising was introduced that includes a synthetic sinogram-based noise simulation tool. The Deep IR method effectively reduces noise in ultra-low dose CT images while preserving image quality through the training of a Convolutional Neural Network (CNN) on simulated noisy sinograms.

Deep learning based techniques can be used in both in prepossessing and post-processing steps. Yin et al., [38] have proposed such a technique known as the progressive

3D residual convolution network (DP-ResNet) in order to improve the whole imaging procedure, namely the conversion of low-dose computed tomography (LDCT) projections into computed tomography (CT) images. The proposed methodology is a two-step approach incorporating sequential network processing in both the image and sinogram domains.

Unrolling techniques combine a learnt prior to the inversion with a conventional iterative approach. These methods resemble traditional methods for tomographic reconstruction optimization. Deep learning is used in each iteration to find the best update, taking into account the result of the former iteration as well as the input from forward operator and its adjoint. In their study, Ding et al., [39] introduced a deep learning approach for reconstructing LDCT images. They utilized a half-quadratic splitting strategy and incorporated a trainable image prior that was based on a framelet filter bank. The method automatically adjusts hyperparameters, requiring only one universal model for processing data acquired at different dose levels. In order to guarantee measurement consistency while repeatedly improving the image, Gupta et al. [40] introduces a new method of image reconstruction that integrates a convolutional neural network (CNN) with projected gradient descent (PGD).

Plug-and-play [41] methods utilize pre-trained denoising algorithms, which are commonly constructed using deep learning or machine learning principles, to function as regularizers within a framework for iterative reconstruction. He et al. [34] developed a novel parameterized 3pADMM algorithm, which optimizes the parameterized plug-and-play (3p) prior and its associated parameters simultaneously within a single framework by integrating deep learning techniques.

Wang et al. [42] introduced an innovative solution called as ADMMBDR algorithm for limited-angle CT. Initially, the ADMM algorithm break down a regularization reconstruction model. Subsequently, integrate a deep convolutional neural network (CNN) within the ADMM framework to reduce artifacts, thus eliminating the need for manually selecting the regularization term and its associated parameter.

Deep learning approaches [6] are widely utilized in CT reconstruction, but a significant drawback is their dependence on large datasets, specifically a set of consisting both low-dose and normal-dose images for supervised learning. Acquiring such image pairings involves costly and time-consuming processes, including two scans and registrations for each projection pair. Moreover, the scarcity of real-world low-dose CT images adds to the challenges. The need for good unsupervised deep learning algorithms [43] for LDCT imaging that can handle situations with less data is thus growing in popularity.

Unal et al. [44] introduced an unsupervised technique tailored for sparse view CT, incorporating the SART reconstruction algorithm and leveraging a deep generative regularizer as a prior. The researchers, Wu et al. [21], proposed an unsupervised learning strategy to train a prior function specifically designed for iterative low-dose CT reconstruction. This approach incorporates K-sparse auto-encoders. Addressing the challenge, the team employed a combination of alternating optimization and sequential quadratic programming (SQP) methods, enhancing them to effectively handle the non-convex nature of the problem. Jiang et al. [45] develop a novel semi-supervised generative technique for accurate super-resolution CT image reconstruction. The approach involves using a deep untrained network with 16 residual blocks as the generator and building a discriminator based on a supervised network.

Liang et al. [46] presented a novel unsupervised model-based deep learning (MBDL) technique for reconstructing low-dose CT (LDCT) images. The MBDL framework is flexible, allowing for the inclusion of supervised training when there are just a few paired NDCT datasets available to assist in optimising network parameters. This allows the framework to operate in a semi-supervised mode.

## III. PROPOSED TECHNIQUE

Inverse problems are inherently ill posed; therefore, prior knowledge must be incorporated into the solution. In general, the regularized least-squares formulation is utilised frequently in image reconstruction process.

$$e^* = \text{argmin}_e \, \|\mathbf{A} - De\|_{l_2}^2 + \lambda R(e) \tag{2}$$

where, Data fidelity $argmin_e \|\mathbf{A} - De\|_{l_2}^2$ term that penalises the $l_2$ distance between measurements which is provided by SART [47] algorithm in the proposed approach. The term "R(.)" is commonly referred to as the regularization term, which serves the purpose of encapsulating prior knowledge regarding the data. The control variable $\lambda$ is employed to regulate the extent to which the regularization term influences the overall solution. This regularization component assumes a vital role in the modeling process by narrowing down the solution space, relying on assumptions grounded in the underlying data. The regularizer is chosen to impose constraints on the solution set in accordance with prior data.

SART is one of the most common iterative techniques. The TV prior is frequently employed as a regularizer $R(e)$ to enforce minimal gradient magnitude (TV norm) in natural images.

TV prior imposes the constraint that a natural image's gradient magnitude (TV norm) must be small. We employ space-variant total variation [48], where $\mu$ is a positive scalar that controls the strength of regularization.

$$WTV(e) \triangleq \sum_{i=1}^{N} \mu || \, [Me] \, ||_2 \tag{3}$$

For a two-dimensional image that is subject to boundary constraints, the operators $M$ is finite difference operations and $Me$ is discrete gradient of $e$ at pixel $i$.

CNN can create a high-quality [49] image from an untrained input vector. Following optimization equation is

used to train deep learning model.

$$\Theta^* = \text{argmin}_\Theta \, L\,(f_\Theta D, e) \tag{4}$$

such that

$$e^* = f_{\Theta^*}(D) \tag{5}$$

where $e^*$ is denoised image, $f_{\Theta^*}$ signifies the CNN parameterized by $\Theta$ and L defines the loss function.

The corresponding optimisation for DIP may be stated within the context of image reconstruction as follows.

$$\Theta^* = \arg\min_\Theta \|\mathbf{D} - \mathbf{A}f_\Theta(\mathbf{z})\|_{l_2}^2 \tag{6}$$

such that

$$\mathbf{e}^* = f_{\Theta^*}(\mathbf{z}) \tag{7}$$

Data fidelity is represented by the term $\|\mathbf{D} - \mathbf{A}f_\Theta(\mathbf{z})\|_{l_2}^2$ in the DIP optimisation problem, with $f_{\Theta*}$ standing in for the unknown image output. The optimisation issue may be formulated using regularized least-squares formulation stated as.

$$\Theta^* = \arg\min_\Theta \left\{ \|\mathbf{D} - \mathbf{A}f_\Theta(\mathbf{z})\|_{\ell_2}^2 + \lambda_{\text{WTV}}\,(f_\Theta(\mathbf{z})) \right\} \tag{8}$$

The constraint counter part of above equation can be represented as:

$$\Theta^* = \arg\min_\Theta \left\{ \|\mathbf{D} - \mathbf{A}f_\Theta(\mathbf{z})\|_{\ell_2}^2 + \lambda_{\text{WTV}}\,(t) \right\} \tag{9}$$

where

$$f_\Theta(\mathbf{z}) = t \tag{10}$$

In order to obtain a low dose image, we will employ an iterative approach to update the weight parameter $\Theta$. This will result in an output $e_k$ that is a function of $\Theta$.

such that

$$e_k = f_{\Theta^*}(D) \tag{11}$$

The output $e_k$ is then multiplied by a sampling mask, with the expectation that it will closely resemble the low dose image. In the context of our undersampling problem, the operator may be described as a binary undersampling mask, which subsequently yields the following operator. In this context, the symbol $\circ$ represents the Hadamard product [50], and the variable $j$ belongs to the set $(0, 1)^{a\times b}$, which represents the binary mask used for the undersampling pattern.

$$e_k^* = f_{\Theta^*}(D) \circ j \tag{12}$$

The value of 1 represents pixels that have been sampled, whereas the value of 0 represents pixels that have been skipped. The multiplication of the estimated CT image by the binary mask ensures that the estimated image aligns with the low-dose image in the sampled regions, preserving data fidelity. The mask is not created randomly in each iteration; rather, it is constant and signifies the particular under-sampling pattern of the low-dose acquisition. This method enables the model to rebuild the complete image while maintaining coherence with the low-dose data.

To solve equation 9, an iterative procedure is required to minimize the equation. This can be achieved by utilizing the ADMM [42] algorithm. The augmented Lagrangian function for this problem can be expressed as

$$\begin{aligned} L(\Theta, t, \lambda) = {} & \|D - \mathbf{A}f_\Theta(z)\|_{\ell_2}^2 + \lambda\,\text{WTV}(t) \\ & + \frac{\beta_t}{2}\|f_\Theta(z) - t\|_{l_2}^2 \\ & + \langle \lambda, f_\Theta(z) - t \rangle \end{aligned} \tag{13}$$

where

$\Theta$ is the optimization variable or weight parameter that is updated during iterative optimization

$t$ is an auxiliary variable, it serves as a reference image from which variations in the reconstructed image are penalized.

$\lambda$ is the dual variable. It is a hyperparameter that regulates the degree of the TV regularization.

The penalization parameter is called $\beta$. It controls the ratio of penalizing deviations from the reference image to fitting the data.

$$\begin{aligned} \Theta_{k+1} = \arg\min_\Theta \Big( & \|D - \mathbf{A}f_\Theta(z)\|_{l_2}^2 \\ & + \frac{\beta_t}{2}\|f_\Theta(z) - t_k + \frac{\beta}{2}\lambda t_k\|_{l_2}^2 \Big) \end{aligned} \tag{14}$$

This step updates the parameters $\Theta$ by minimizing the data fidelity term and the penalty term that ensures $f_\Theta(z)$ is close to $t_k - \frac{\beta}{2}\lambda t_k$

The first part of the $\|D - \mathbf{A}f_\Theta(z)\|_{l_2}^2$ equation is data-fidelity term ensuring that the reconstructed image $f_\Theta(z)$ matches the given measurements D as closely as possible. The second part is a regularization term. It introduces a penalty for solutions that deviate from the previous auxiliary variable $t_k$. and the dual variable $\lambda_k$. This helps to incorporate prior knowledge or constraints on the solution.

$$\begin{aligned} t^{k+1} = \arg\min_t \Big( & \lambda\,\text{WTV}(t) \\ & + \frac{\beta_t}{2}\left\| f_{\Theta^{k+1}}(z) - t + \frac{1}{\beta_t}\lambda_t^k \right\|_{l_2}^2 \Big) \end{aligned} \tag{15}$$

The term $\sum_{i=1}^{N} \mu_k i \, \|t_i\|_2^2$ represents a regularization on the auxiliary variables $t_i$. This term encourages sparsity in the auxiliary variables and helps to refine the solution. The other half of the equation ensures that the auxiliary variable aligns with the measurements. It introduces a penalty if the auxiliary variable deviates from the current estimate of the reconstructed image.

$$\lambda_t^{k+1} = \lambda_t^k + \beta_t \left( f_{\Theta^{k+1}}(z) - t^{k+1} \right) \tag{16}$$

The equation modifies the dual variable $\lambda$ on each iteration by considering the discrepancy between the reconstructed image and the updated auxiliary variable. The equation

updates the dual variable $\lambda$ based on the difference between the current estimate of the reconstructed image $f_{\Theta^{k+1}}(z) - t^{k+1}$ and the updated auxiliary variable $t^{k+1}$. The dual variable plays a role in enforcing coherence among the reconstructed image and the auxiliary variables.

## IV. RESULT AND DISCUSSION

In this section we will discuss the experiential results performed, regularization strategies used in the experimental process.

### A. RECONSTRUCTION STRATEGIES

The center of our approach is DIP, which does not require a large dataset of labeled images for training. The network architecture naturally favors the generation of realistic image structure over noise. This allows the network to serve as a powerful regularizer, guiding reconstruction toward a more accurate image without needing ground truth data. The network learns the input data alone. In our proposed method, the DIP network acts as a regularizer due to its architecture and various losses, which help guide the model toward reconstructing noise-free images. All the loss functions used in this approach follow an unsupervised adaption. This approach combines elements of conventional image reconstruction methods with the utilization of a neural network acting as image prior. The optimization process involves iteratively refining the latent vector and weights to enhance the consistency between generated and actual image based on specified measurements. The reconstruction idea is to optimize the loss of randomly initialized neural network in such a way that NN act as a prior without the need of any training and testing. The iterative fusion of SART and Deep Convolutional Neural network is displayed in Figure 1. The first module is reconstruction module it generates an initial low dose CT image using the SART algorithm. This act as a starting point for the succeeding modules. The second module is the Neural Network Module, in this module network is initialized with random noise image (Gaussian noise). The random image has the same dimensions as the image generated by SART. Networks estimates what the image is, and then they multiply that guess by a binary mask. In our case, we used a Hadamard matrix. The resultant multiplied image is used to figure out different types of loss, like perceptual loss, SSIM loss and $l_2$ loss. Perceptual loss capture more complex visual details and structures. The major emphasis of $l_2$ loss is the pixel-by-pixel disparities between the estimated and reconstructed images. Where its main intent is to cut-down the overall mean squared error, guaranteeing a close match between the reconstructed low dose image and the estimated image in terms of pixel intensities and SSIM loss ensures the structure similarities between estimated image the reconstructed low-dose image. For maintaining the unsupervised characteristics of SSIM loss rather than comparing the output to a labeled ground truth image, the SSIM loss compares the generated image with an initial estimate obtained through SART and product of Hadamard product. This resulatnt image $e'_k$ is generated directly from the input data itself, not from external labels or pre-trained models, thus maintaining the unsupervised nature of the method.

$$L_{\text{SSIM}}(e_0, e_k^*) = (1 - SSIM\left(e_0, e_k^*\right)) \tag{17}$$

Here $L_{\text{SSIM}}$ is structural similarity, $e_0$ image estimated by SART reconstruction algorithm, $e_k^* = f_{\Theta^*}(D) \circ j$

The $l_2$ loss emphasizes the pixel-by-pixel disparities between the reconstructed image and the input data (such as noisy or incomplete observations). Its primary intent is to ensure a close match between the reconstructed image and the input observations regarding pixel intensities without requiring a ground truth image, or labeled data. $l_2$ loss is given as

$$L_{l_2}(e_0, e_k^*) = \sum_{i=1}^{N} \left(\phi_l(e_0)_i - \phi_l(e_k^*)_i\right)^2 \tag{18}$$

where $e_0$ is image generated by SART, with total number of iteartions equal to 40. And $e_k^*$ is image obtained from NN and Hadamard product. Here $l_2$ loss maintains the unsupervised characteristics.

$$L_{\text{perceptual}}(f_\Theta(z) \circ j, e_0) = \sum_{l} \|\phi_l(f_\Theta(z)) - \phi_l(e_0)\|_2^2 \tag{19}$$

Here $f_\Theta(z)$ is output of neural network $f$ parameterized by $\Theta$, $e_0$ is reference image. $\phi_l$ denotes the feature maps extracted from the $l - th$ layer of a pre-trained network, here we have used VGG-19. The reference image $e_0$ is not a labeled ground truth image but rather derived from the SART.

In the third module Weighted TV Loss Module used to calculate weighted TV loss among the predicted (Initial estimated image) image and the reconstructed low-dose image. This encourages the network to produce images with minimal variation while staying close to the initial reconstruction. TV loss is applied to reduce noise and encourage smoothness in the reconstructed image, a common goal in image reconstruction tasks. For unsupervised adaption, this loss operates directly on the generated image without any comparison to labeled data. It simply regularizes the image's gradient to promote smoothness, a feature common in unsupervised methods.

$$L_{\text{WTV}} = \text{WTV}\left(f_\theta(z)\right) \tag{20}$$

The fourth module contains weighted Sinogram loss or measurement loss between initial Sinogram data generated by NN and original Sinogram data. The projection loss is here used to measure of the discrepancy between the measured projection data and the simulation generated projection data. We enforce consistency between the reconstructed and the raw data, making this unsupervised. Also, we are not providing labeled data to ensure that the proposed loss adapts to the unsupervised characteristics.

$$L_{\text{Sinogram Loss}} = \|D - \mathbf{A}f_\Theta(z)\|_{l_2}^2 \tag{21}$$

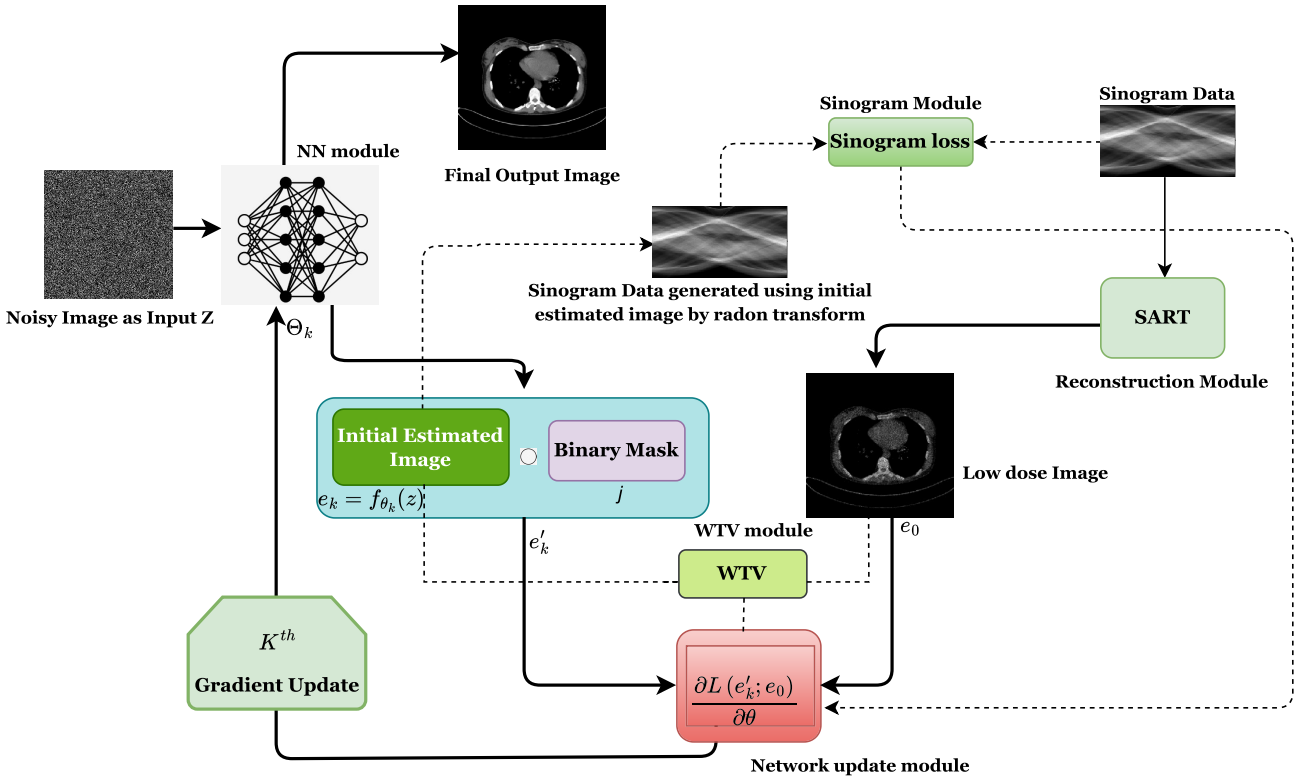


**FIGURE 1.** Working of the proposed Technique.

The fifth module is Network Update Module this module utilizes the calculated loss functions to update the network parameters and fine-tunes the network's ability to generate images that align with both the low-dose CT image and the original sinogram data.

### B. NETWORK ARCHITECTURE AND EXPERIMENTAL SETUP

The CNN design utilised in all tests is depicted in Figure 2, which is a modified version of the U-net architecture first suggested by [49]. Specifically, the popular U-net architecture is modified to include a convolutional layer in the skip connections. The proposed network consists of two parts the left is encoding path and right part is decoding path. The encoded region is like a standard CNN architecture, that consists of two convolational layes of $3 \times 3 \times 3$, succeeded by batch normalization (BN) and a leaky rectified linear unit (LReLU) as activation. Additionally, a $3 \times 3 \times 3$, 3D downsampling convolution layer with a stride of two is applied, succeeded by the BN and the LReLU. Additionally, the number of feature channels doubles with each round of downsampling. The decoding path includes a $3 \times 3 \times 3$ deconvolution layer, Batch Normalization (BN), Leaky Rectified Linear Unit (LReLU), upsampling, skip connection with the matching linked feature map from the encoding path, and two $3 \times 3 \times 3$ convolution layers, each succeeded by BN and LReLU. The Adam optimizer employed in this case. As the input moves farther into the network, this structure causes the network's functional receptive field to grow. Furthermore, use of skip connections allows future layers to effectively rebuild feature maps by including both local and global texture information. The experimental configuration consisted of the NVIDIA RTX A4000, a 16 GB Graphics Processing Unit (GPU), an Intel Xeon Gold Processor 6142 with a maximum turbo frequency of 3.70 GHz, and 32 GB of RAM.

### C. RESULTS ON REAL DATASET

The real dataset known as the dead piglet dataset, which was published by Yi and Babyn [54], is utilized to assess the denoising performance of the suggested DL model.

This data set provides CT images at different doses by reducing the tube current from 300 mA to 150mAs, 75mAs, and 15mAs. Accordingly, in this study, the CT images obtained at 300mAs were considered the Regular dose (RDCT) or Full dose CT (FDCT) dataset and the rest the Low dose dataset (LDCT) datasets. Also, these three LDCT piglet data sets consisting of 150mAs, 75mAs, and 15mAs are labelled as half dose, quarter dose, and ultra-low dose data sets.

Figure 3 presents results from the piglet dataset at a dose level of 150 mAs and tube current of 100 kV. Figure 4 shows results at 75 mAs with the same tube current of 100 kV, and Figure 5 shows results at 15 mAs, also with a tube current of

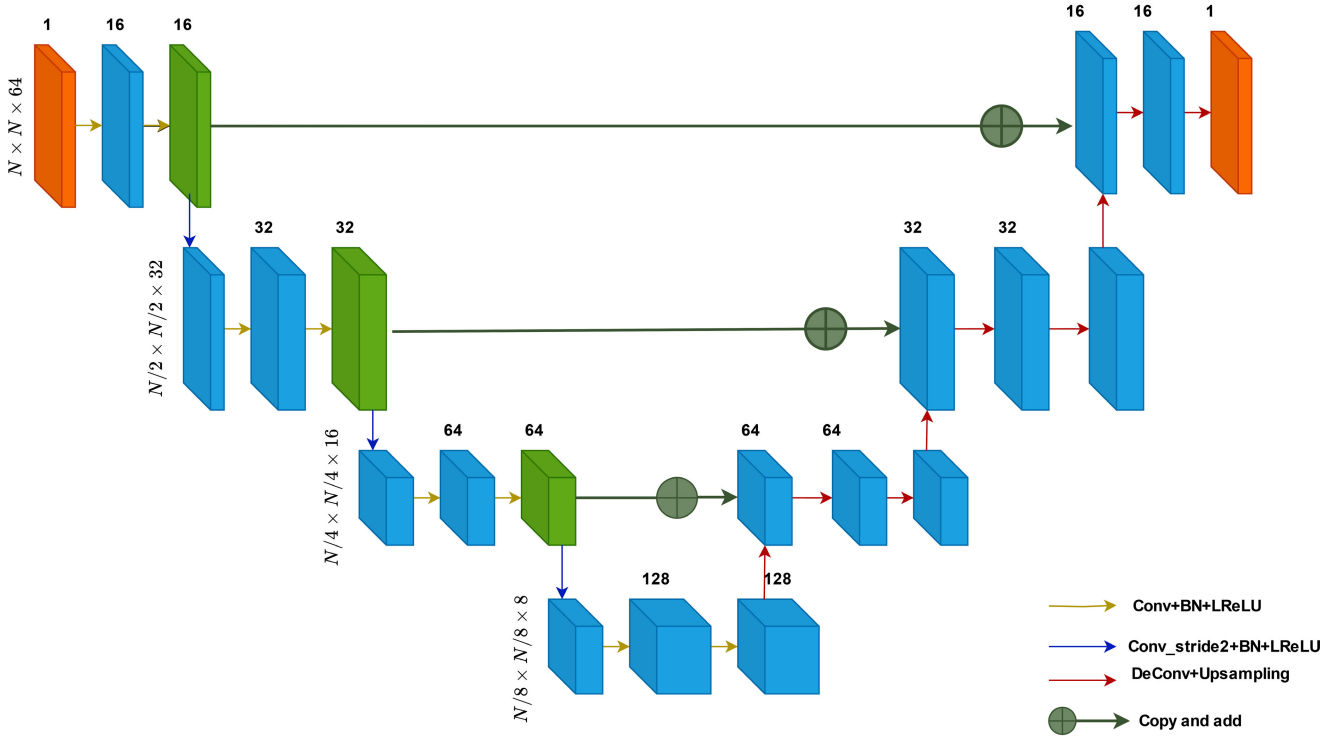


**FIGURE 2.** Neural network Architecture used in the proposed approach. Total number of channels (N = 512) are depicted on the top of each box and pixel size are displayed on the left. Arrows are used for displaying different set of operations.

100 kV. The display window for all experiments is set to [40, 350] HU.

### D. CLINICAL DATA RECONSTRUCTION

In order to evaluate the suggested technique in practical situations, a clinical images facilitated by Mayo Clinics for the 2016 NIH-AAPM-Mayo Clinic Low Dose CT Grand Challenge [30] was utilized. Results obtained for Mayo-clinic dataset is shown in Figure 6, 7 the window size for all experiments is set as [−160 to 240]. In Figure 6, the image shown is of a patient with a lesion. Data obtained at 120 kV and 200 quality reference mAs (QRM) is termed as Full Dose (FD) data, while simulated data that corresponds to 120 kV and 50 QRM is referred as Quarter Dose (QD) or Low-Dose CT (LDCT) data. In Figure 7, the image shown is of a patient with a lesion.

### E. METHODS IN COMPARISON

To evaluate the performance of the suggested approach, it is compared with other existing techniques like BM3D [51], SwinCT [52], DIP+TV [53], Dataset free learning [55], Proj2Proj [56].

Total number of iterations selected are 400 with Adam optimizer is utilized. The proposed method is compared with various reconstructed methods LDCT (QD), BM3D, SwinCT, DIP+TV, Dataset Free learning and Proj2Proj. In low-dose CT (LDCT) imaging, a reduction in dose generally results in increased noise, which considerably impairs overall image quality. Traditional denoising methods such as BM3D are effective in noise suppression; however, they frequently result in over-smoothing, which causes a significant loss of the structural details in the image. SwinCT, a supervised technique, seeks to improve structural details; however, it sometimes exhibits a lack of clarity in finer image elements. The unsupervised DIP+TV method demonstrates potential by effectively preserving the majority of structural information, although certain subtle details remain unclear. At the half dose (150mAS) dose level, the proposed technique demonstrated a PSNR of 37.2240 and an SSIM of 0.9613, surpassing Proj2Proj, which achieved a PSNR of 35.8921, and Dataset Free Learning, which attained a PSNR of 35.7362. While Proj2Proj and Dataset Free Learning produced visually appealing outcomes, the proposed method demonstrated superior structural preservation. At the 75 mAs dose level, our method attained a PSNR of 36.751, in contrast to 35.5910 for Proj2Proj and 35.0411 for Dataset Free Learning. At the 15 mAs dose, Proj2Proj and Dataset Free Learning demonstrated performance comparable to our method regarding PSNR and SSIM metrics. This analysis demonstrates the proposed method's balanced performance across dose levels, showcasing superior structural preservation and image clarity. The proposed method attained a maximum PSNR of

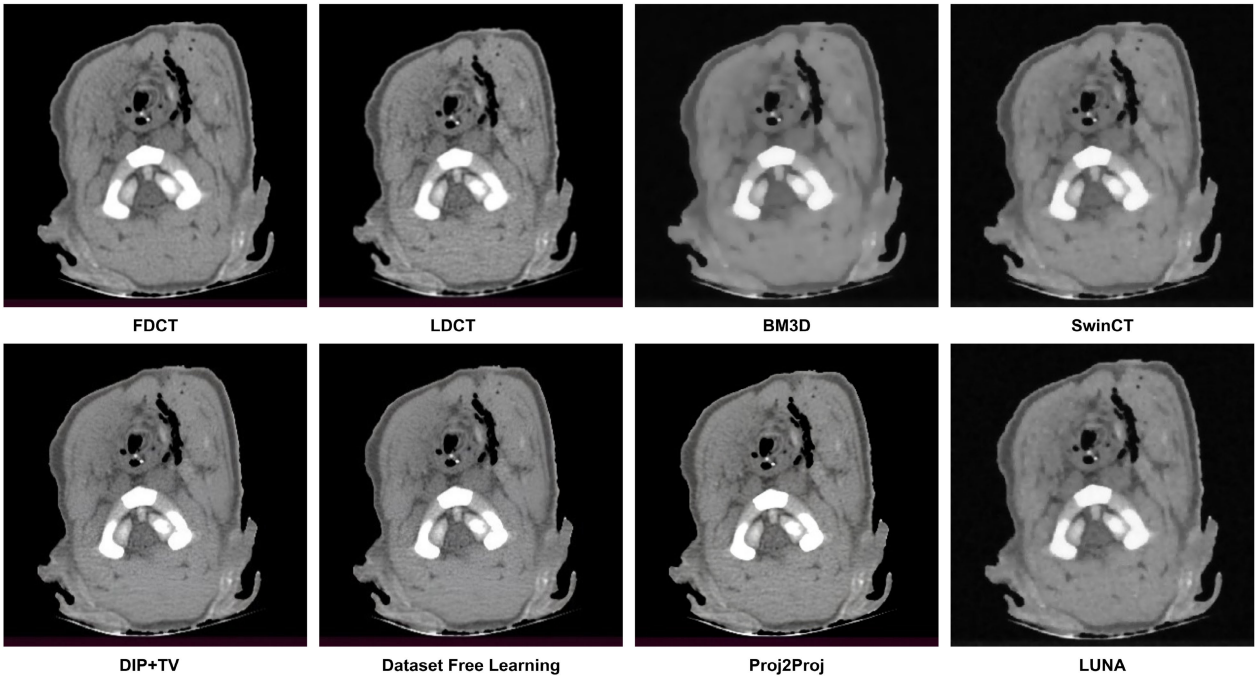


(a) Comparative Analysis of Visual Performance

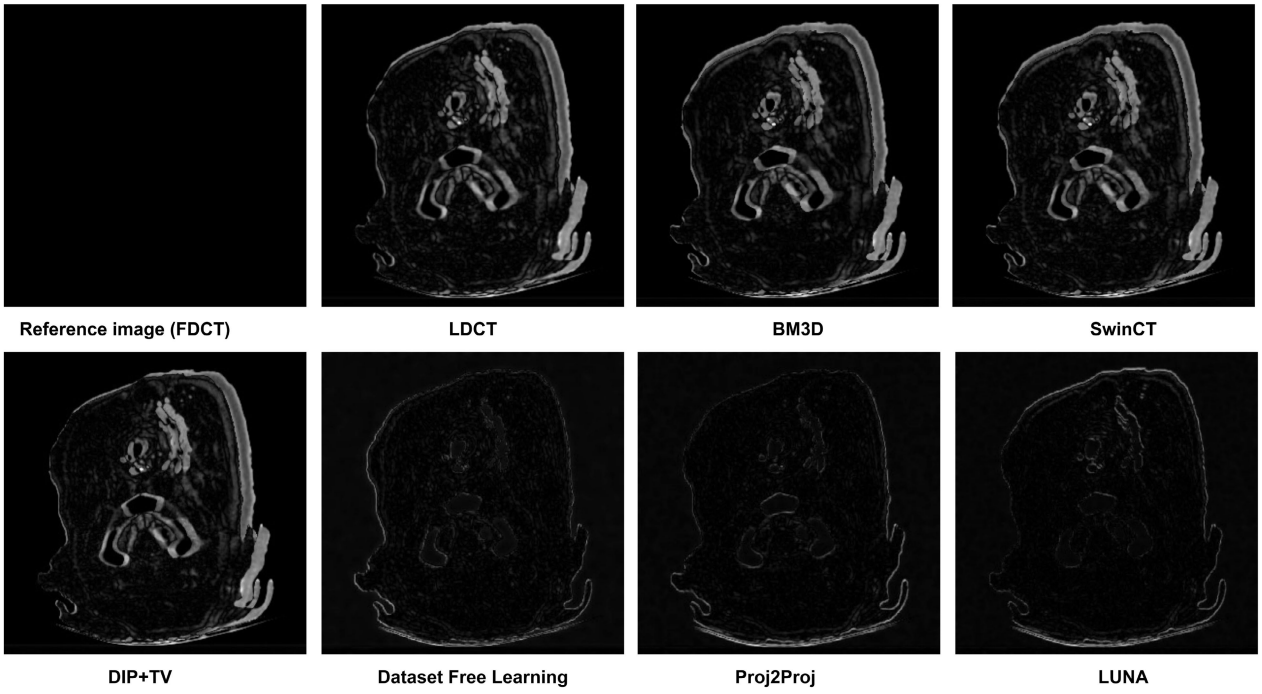


(b) Difference Map

**FIGURE 3.** Comparative analysis of visual performance and Difference map of various techniques on piglet dataset on dose level 150mAs. The images are arranged from top to bottom in the order: FDCT, LDCT, BM3D [51], SwinCT [52], DIP+TV [53], Dataset Free Learning [55], Proj2Proj [56], and LUNA.

37.500 and a structural similarity index of 0.9629 for the Mayo Clinic dataset. Figures 6 and 7 illustrate that Dataset Free Learning and Proj2Proj yield visually promising results; nevertheless, certain finer details are compromised in their

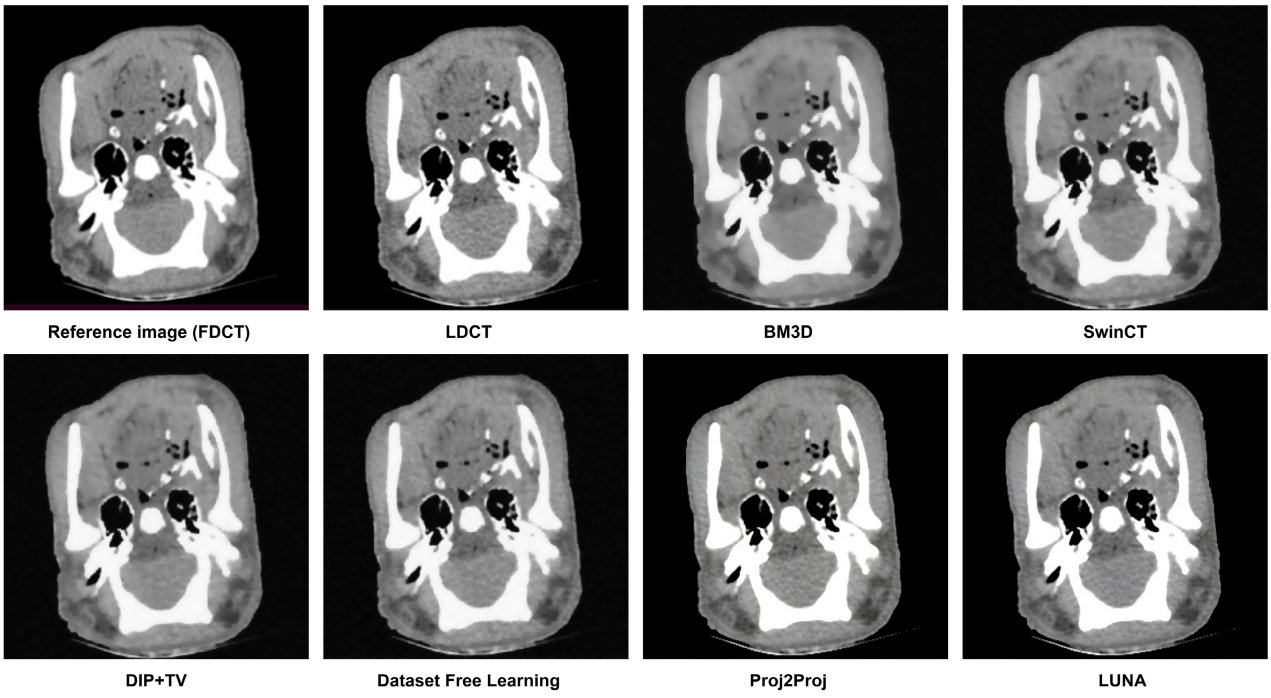


(a) Comparative Analysis of Visual Performance

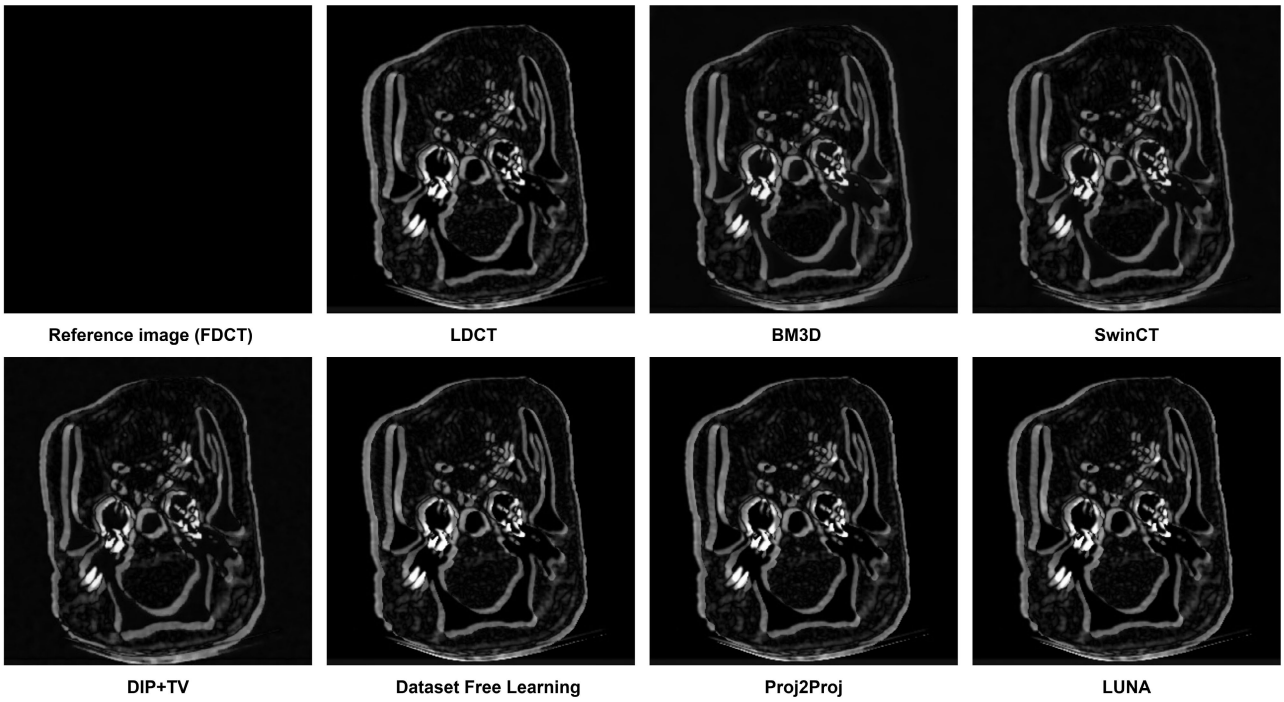


(b) Difference Map

**FIGURE 4.** **Comparative analysis of visual performance and Difference map of various techniques on piglet dataset on dose level 75mAs. The images are arranged from top to bottom in the order: FDCT, LDCT, BM3D [51], SwinCT [52], DIP+TV [53], Dataset Free Learning [55], Proj2Proj [56], and LUNA.**

reconstructions. Our method exhibits enhanced capability in maintaining intricate structural details. The proposed method effectively balances noise reduction and detail preservation, resulting in high-quality images that clearly display both

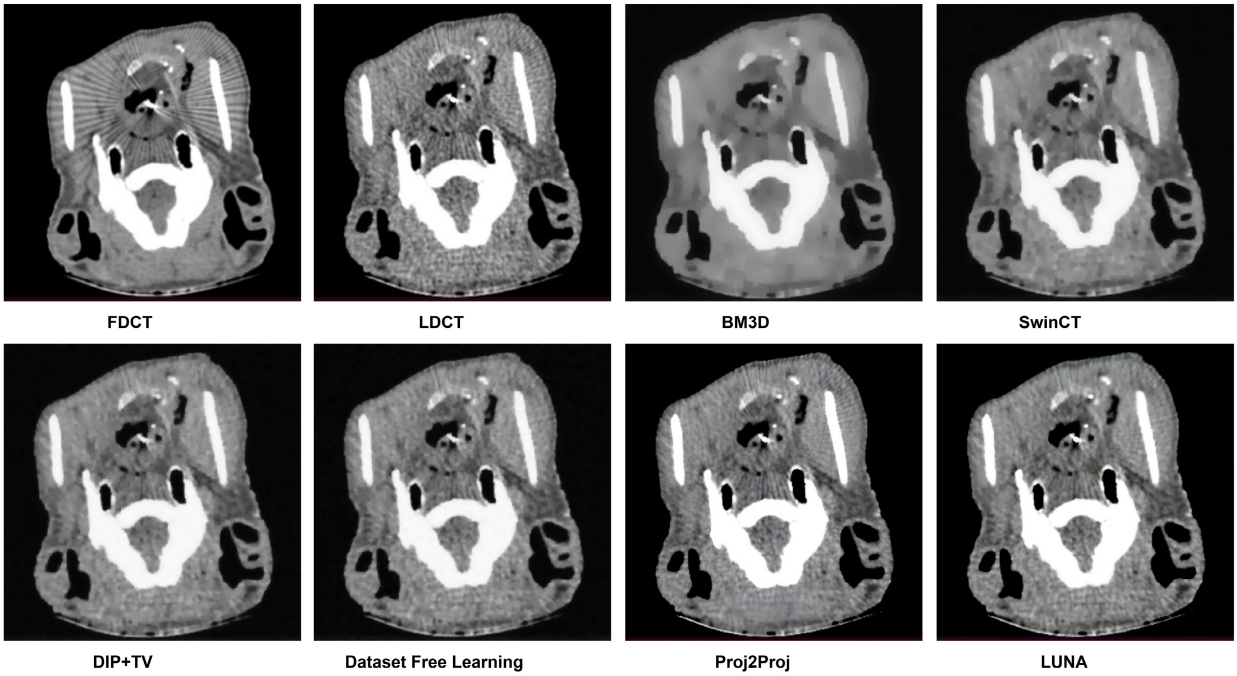


(a) Comparative Analysis of Visual Performance

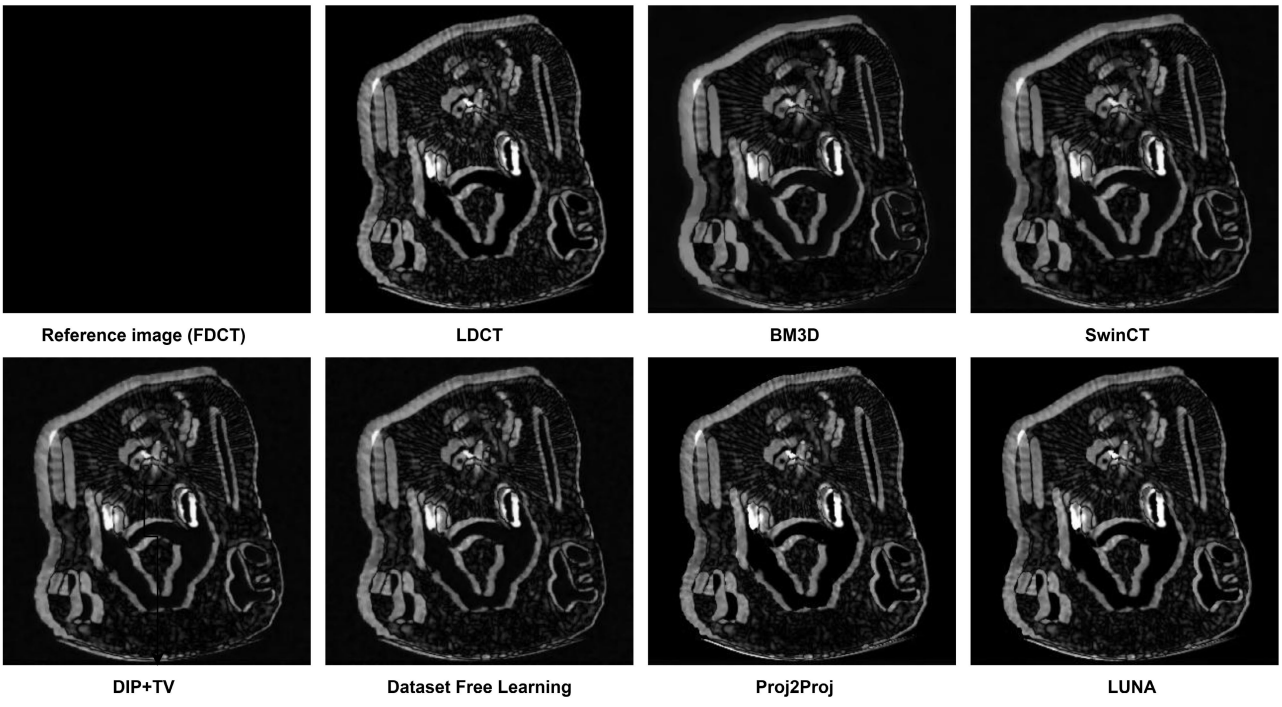


(b) Difference Map

**FIGURE 5.** **Comparative analysis of visual performance and Difference map of various techniques on piglet dataset on dose level 15mAs. The images are arranged from top to bottom in the order: FDCT, LDCT, BM3D [51], SwinCT [52], DIP+TV [53],Dataset Free Learning [55], Proj2Proj [56], and LUNA.**

major structural details and finer elements. This indicates the effectiveness and advantages of the proposed method in preserving both structural integrity and fine details in reconstructed images.

**TABLE 1.** Comparison of evaluation metrics using the piglet data-set with state-of-art methods.

| Images | Metrics | LDCT | BM3D [51] | SwinCT [52] | DIP+TV [53] | Dataset Free Learning [55] | Proj2Proj [56] | LUNA |
|---|---|---|---|---|---|---|---|---|
| Image 1 (150mAs) | **PSNR** | 27.0813 | 28.037 | 32.9392 | 35.1275 | 35.7362 | 35.8921 | 37.2240 |
| | **SSIM** | 0.8980 | 0.9037 | 0.9332 | 0.94377 | 0.9600 | 0.9612 | 0.9613 |
| Image 2 (75mAs) | **PSNR** | 28.823 | 30.822 | 33.927 | 34.8317 | 35.0411 | 35.5910 | 36.751 |
| | **SSIM** | 0.8915 | 0.8221 | 0.9107 | 0.9304 | 0.9345 | 0.9372 | 0.9471 |
| Image 3 (15mAs) | **PSNR** | 24.7314 | 25.1471 | 28.1465 | 29.7908 | 30.3543 | 30.5321 | 32.6533 |
| | **SSIM** | 0.9039 | 0.9127 | 0.93731 | 0.9413 | 0.9423 | 0.9452 | 0.9474 |

**TABLE 2.** Comparison of evaluation metrics using the Mayo-clinic data-set with state-of-art methods.

| Images | Metrics | LDCT | BM3D [51] | SwinCT [52] | DIP+TV [53] | Dataset Free Learning [55] | Proj2Proj [56] | LUNA |
|---|---|---|---|---|---|---|---|---|
| Image 1 | **PSNR** | 28.0813 | 29.037 | 33.9392 | 35.9275 | 36.1553 | 36.4571 | 37.500 |
| | **SSIM** | 0.9080 | 0.9107 | 0.9332 | 0.94377 | 0.9580 | 0.9591 | 0.9624 |
| Image 2 | **PSNR** | 27.813 | 28.832 | 32.927 | 34.2317 | 35.0244 | 35.2100 | 36.751 |
| | **SSIM** | 0.9115 | 0.9124 | 0.9342 | 0.9501 | 0.9508 | 0.9553 | 0.9571 |
| Image 3 | **PSNR** | 30.7314 | 31.1471 | 33.1567 | 34.5198 | 35.0965 | 35.9902 | 36.2079 |
| | **SSIM** | 0.9012 | 0.9122 | 0.9331 | 0.9413 | 0.9501 | 0.9567 | 0.9601 |
| Image 4 | **PSNR** | 28.813 | 29.832 | 33.927 | 34.4407 | 35.3452 | 35.6410 | 35.6751 |
| | **SSIM** | 0.9149 | 0.9283 | 0.9434 | 0.9542 | 0.9581 | 0.9589 | 0.9591 |

**TABLE 3.** PSNR and SSIM values estimated by changing the weights of the various loss functions used in the experiments.

| Sinogram loss | perceptual loss | WTV loss | WSSIM loss | W$l_2$ loss | Beta_t | PSNR | SSIM |
|---|---|---|---|---|---|---|---|
| 0.5 | 0.2 | 0.1 | 0.2 | 1 | 10 | 25.5 | 93.5 |
| 0 | 0 | 0 | 0 | 1 | 50 | 26.5 | 93.7 |
| 0.2 | 0 | 0 | 0 | 0 | 50 | 24.5 | 92.5 |
| 0.4 | 0.2 | 0.2 | 0.2 | 0.5 | 50 | 33.4 | 95.7 |
| 1 | 1 | 1 | 1 | 1 | 50 | 37.5 | 96.99 |

The values in Table 3 represent the weights assigned to different loss functions used in our experiments. We provided multiple sets of these weights to assess their impact on the model's performance. The table illustrates how adjusting

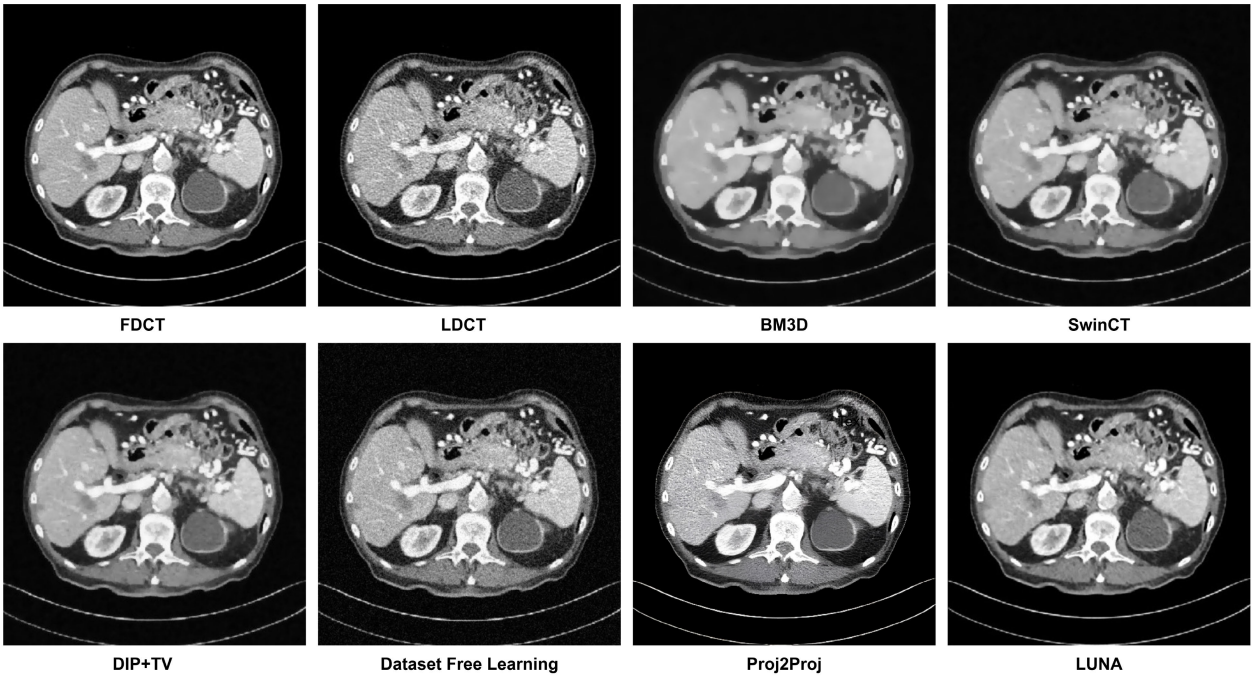


(a) Comparative Analysis of Visual Performance

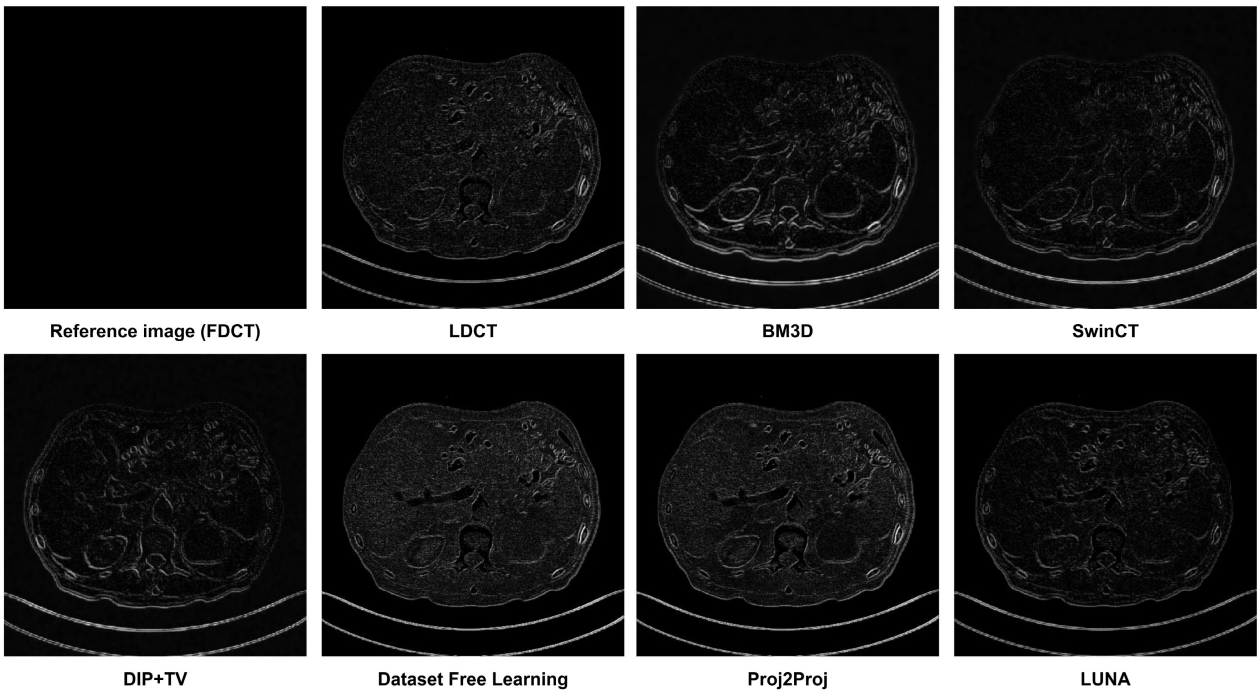


(b) Difference Map

**FIGURE 6.** **Comparative analysis of visual performance and Difference map of multiple techniques on a Mayo Clinic dataset image having lesion in liver. The images are arranged from top to bottom in the order: FDCT, LDCT, BM3D [51], SwinCT [52], DIP+TV [53], Dataset Free Learning [55], Proj2Proj [56], and LUNA.**

these weights influences the PSNR and SSIM metrics. The loss functions incorporated in our experiments include sinogram loss, perceptual loss, WTV loss, WSSIM loss, and $l_2$ loss. The weights of these loss functions are

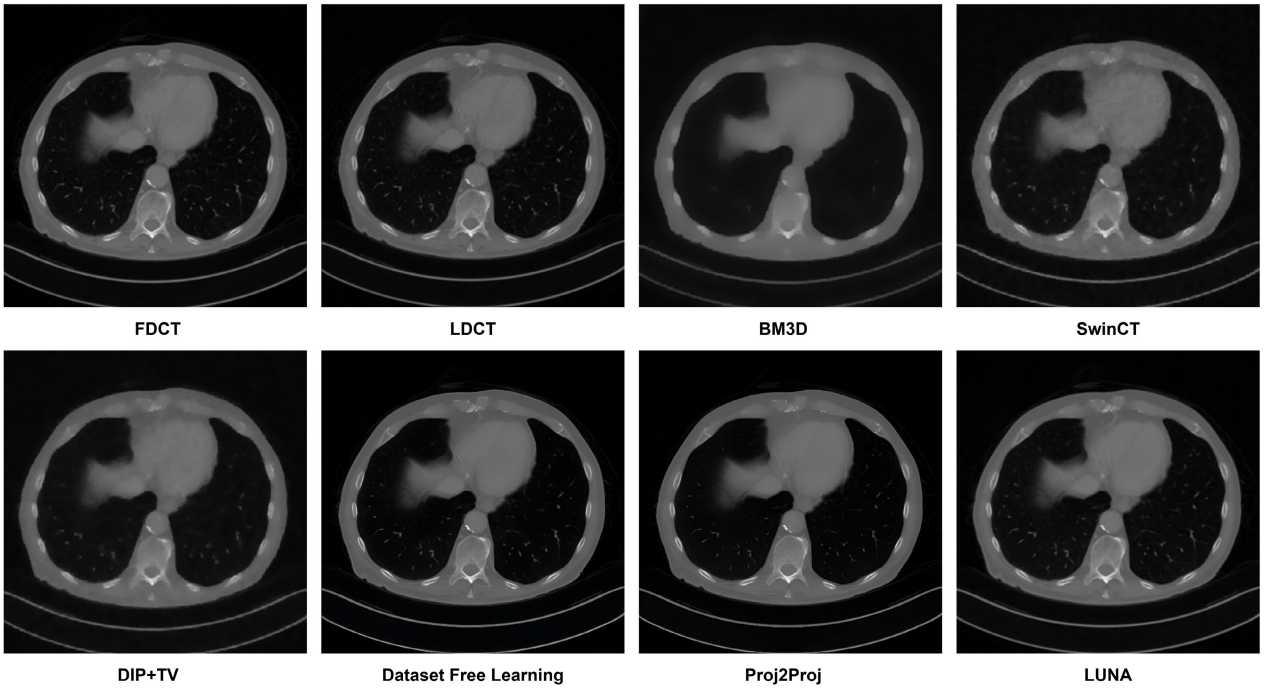


(a) Comparative Analysis of Visual Performance

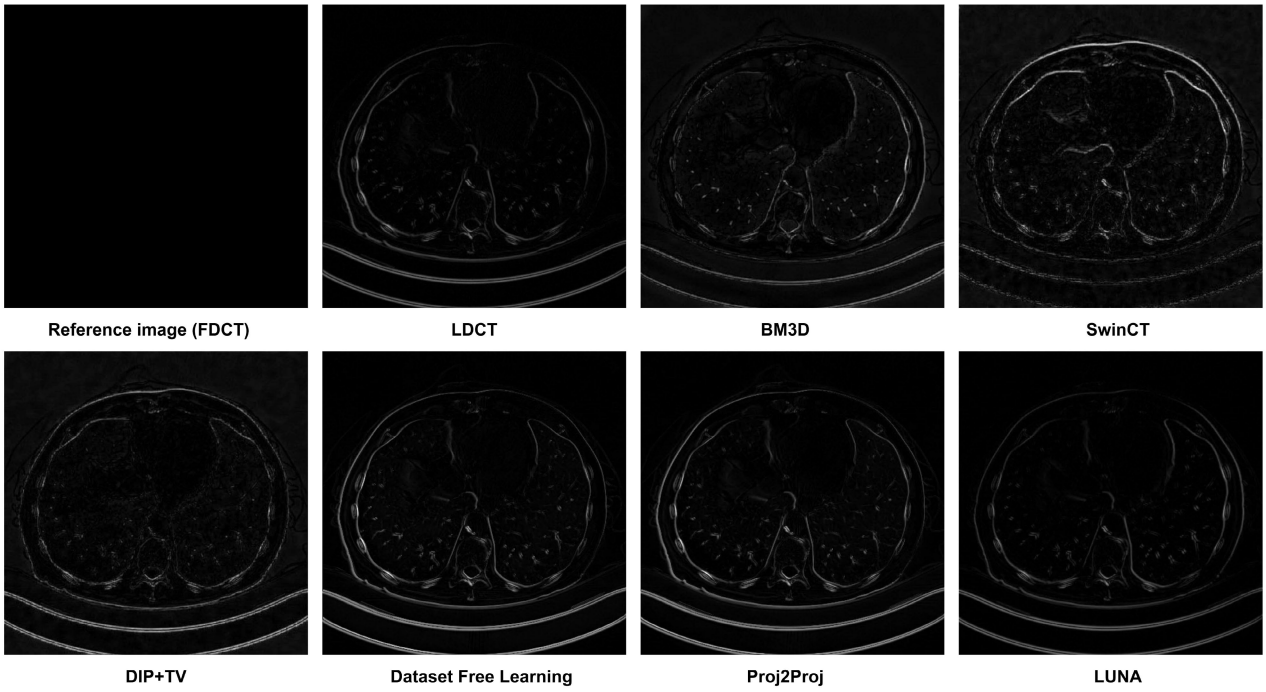


(b) Difference Map

**FIGURE 7.** **Comparative analysis of visual performance Difference map of multiple techniques on a Mayo Clinic dataset of Lung image. The images are arranged from top to bottom in the order: FDCT, LDCT, BM3D [51], SwinCT [52], DIP+TV [53], Dataset Free Learning [55], Proj2Proj [56], and LUNA.**

tuned randomly throughout experimentation to obtain the best possible performance. Additionally, we used $\beta$ as a penalty parameter; this helps enforce consistency between the subproblems of the ADMM framework, stabilizing and

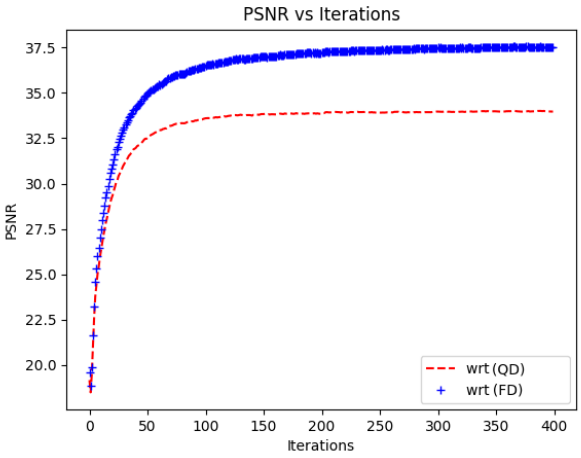


(a) PSNR vs Iterations

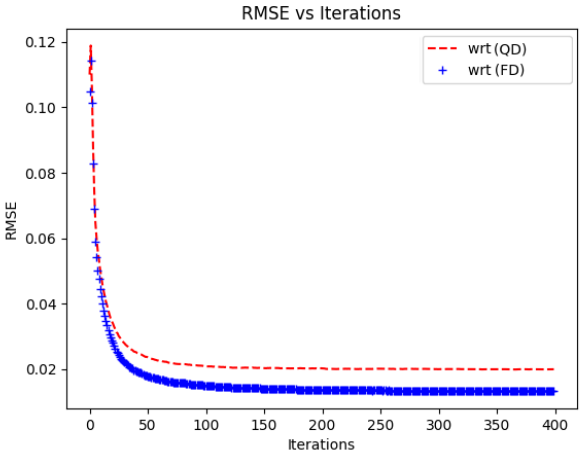


(b) RMSE vs Iterations

**FIGURE 8.** PSNR and RMSE values along with number of iterations.

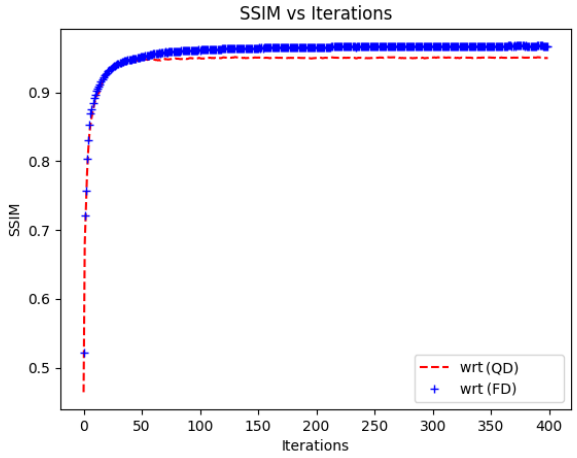


(a) SSIM vs iterations

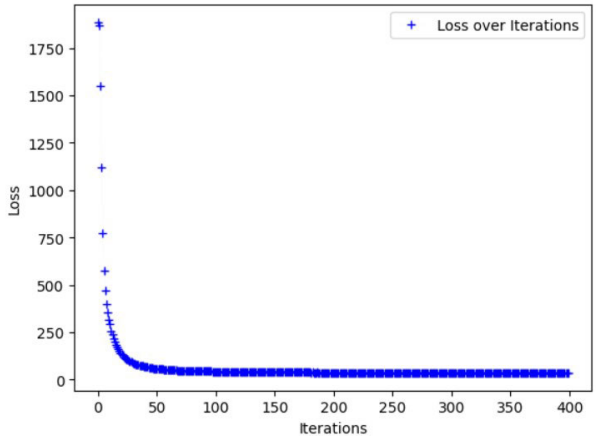


(b) Loss over iterations

**FIGURE 9.** SSIM and Loss values along with number of iterations.

improving the convergence during image reconstruction. These losses collectively contribute to the network's overall performance. The significance of these weights is discussed in the section on reconstruction strategies.

The proposed technique has 2,272,649 parameters and a run time of 55 minutes per image. Initially, the network calculates the total cost or loss, aiming to minimize it throughout the optimization process. As the figure demonstrates, increasing the number of iterations leads to a significant decrease in the network's loss, while simultaneously increasing the PSNR value, indicating improved image quality. The reconstruction quality of the generated images is assessed by comparing them with Full Dose (FD) and Half Dose (QD) reference images. Notably, the network achieves satisfactory results after only 355 iterations. Initially, the PSNR values exhibit a rapid radial increase, indicating substantial improvement. This observation highlights the remarkable performance of our network, achieving significant improvement rapidly and maintaining high quality throughout the iterative process. However, after the 300th iteration, the rate of increase starts to slow down, indicating a phase of diminishing returns. So we decide to stop after 400 iterations. The obtained results emphasizes the excellent performance of our network, achieving significant improvement quickly and maintaining good quality throughout the iterative process. Based on our experimental observation, it has been found that unsupervised methods are highly effective and can successfully mitigate the requirement for a large amount of data.

The success of our proposed unsupervised framework relies on the dynamic interaction of network weights across various configurations. Table 3 displays the different weight values assigned to the network. We performed a thorough analysis comparing the quality of image reconstruction in scenarios with full dose and quarter dose. The graphical representation showcases the fine outcomes obtained. Figure 8 (a) displays the values for PSNR versus iterations, while Figure 8 (b) shows the RMSE versus iterations. Figure 9 (a) displays the SSIM values plotted against iterations, while Figure 9 (b) showcases the loss values plotted

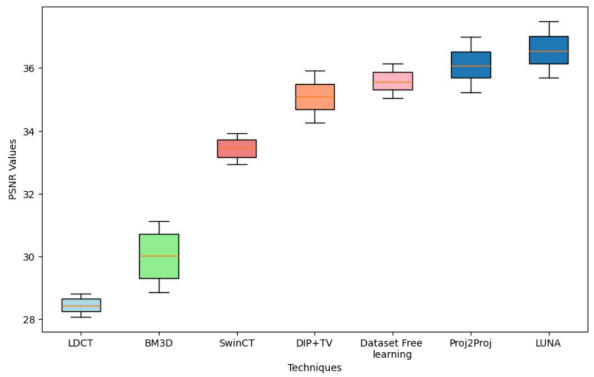


(a) Assessment of the proposed technique's performance based on PSNR values with existing techniques.

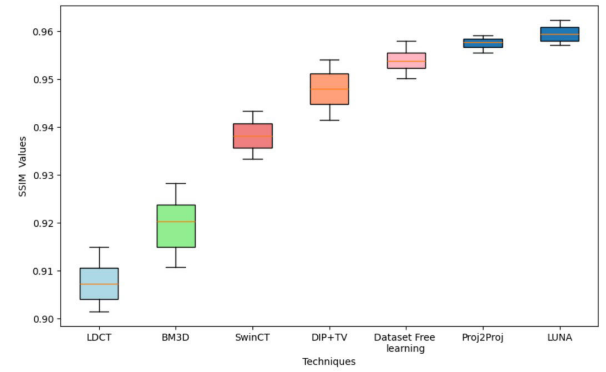


(b) Assessment of the proposed technique's performance based on SSIM values with existing techniques.

**FIGURE 10. PSNR and SSIM values assessment with existing techniques.**

against iterations. The assessment of proposed techniques based on PSNR and SSIM values is shown in the Figure 10. Based on the graph of PSNR vs Iterations, it is visible that the initial PSNR value is 18.500 and the SSIM value is 0.680. Additionally, the loss value is recorded as 1868.64953. The loss value experiences a significant decrease, while the PSNR value shows a notable increase of 27.323 at iteration 10. The corresponding loss value is 291.80734, and the ssim value is 0891. After reaching iteration 50, the PSNR value obtained is 34.937 and the SSIM value is 0.948. After 50 iterations, there is a gradual improvement in the PSNR value, as shown in Figure 5. After 120 iterations, we achieved a PSNR value of 36.760 and an SSIM value of 0.951. At 355 iterations, we obtain a PSNR value of 37.503. After this iteration, there is only a slight increase in the PSNR value, so we decide to stop at 400 iterations.

The reconstructed image quality achieved a score of 37.5 dB for FD and 33.5 dB for QD. In addition, our approach demonstrated significant improvements with the Structural Similarity Index Measure (SSIM) values reaching 97.13 for FD and 96.24 for QD, highlighting its effectiveness.

For optimal results, it is recommended to configure the Sinogram loss, perceptual loss, weighted TV loss, Weighted SSIM loss, weighted norm2 loss,Beta, and learning rate lambda with the following values: Sinogram loss = 1, perceptual loss = 1, weighted TV loss = 1, SSIM loss = 1, weighted L2 loss = 1, Beta = 50, and learning rate $\lambda = 0.1$.

## V. CONCLUSION AND FUTURE WORK

In this paper an efficient approach for low-dose CT reconstruction technique is proposed. A hybrid approach is developed where the SART reconstruction algorithm is integrated with a Deep Convolutional Neural Network (Deep CNN) serving as a prior. This approach leverages the effectiveness of Deep Convolutional Neural Networks in identifying significant patterns within the dataset, hence reducing the reliance on extensive training data, which is often a constraint on the effectiveness of deep learning methods. The suggested technique exhibits superior performance compared to conventional reconstruction methods.

In future research, efforts will be made to integrate a wider range of loss functions and reduce the overall number of iterations. The clinical usability, an additional criterion used to evaluate the reconstruction of medical images, can be further examined by the domain experts to validate the proposed approach.

## REFERENCES

[1] K. T. Smith and F. Keinert, "Mathematical foundations of computed tomography," *Appl. Opt.*, vol. 24, no. 23, p. 3950, Dec. 1985, doi: 10.1364/ao.24.003950.

[2] W. Huda and A. Vance, "Patient radiation doses from adult and pediatric CT," *Amer. J. Roentgenol.*, vol. 188, no. 2, pp. 540–546, Feb. 2007, doi: 10.2214/ajr.06.0101.

[3] W. R. Hendee and F. M. Edwards, "ALARA and an integrated approach to radiation protection," *Seminars Nucl. Med.*, vol. 16, no. 2, pp. 142–150, Apr. 1986, doi: 10.1016/s0001-2998(86)80027-7.

[4] D. Zeng, J. Huang, Z. Bian, S. Niu, H. Zhang, Q. Feng, Z. Liang, and J. Ma, "A simple low-dose X-ray CT simulation from high-dose scan," *IEEE Trans. Nucl. Sci.*, vol. 62, no. 5, pp. 2226–2233, Oct. 2015, doi: 10.1109/TNS.2015.2467219.

[5] M. J. Willemink, P. A. de Jong, T. Leiner, L. M. de Heer, R. A. J. Nievelstein, R. P. J. Budde, and A. M. R. Schilham, "Iterative reconstruction techniques for computed tomography part 1: Technical principles," *Eur. Radiol.*, vol. 23, no. 6, pp. 1623–1631, Jan. 2013, doi: 10.1007/s00330-012-2765-y.

[6] L. R. Koetzier, D. Mastrodicasa, T. P. Szczykutowicz, N. R. van der Werf, A. S. Wang, V. Sandfort, A. J. van der Molen, D. Fleischmann, and M. J. Willemink, "Deep learning image reconstruction for CT: Technical principles and clinical prospects," *Radiology*, vol. 306, no. 3, Mar. 2023, Art. no. e221257, doi: 10.1148/radiol.221257.

[7] J. Wang, H. Lu, T. Li, and Z. Liang, "Sinogram noise reduction for low-dose CT by statistics-based nonlinear filters," *Proc. SPIE*, vol. 5747, pp. 2058–2066, Apr. 2005, doi: 10.1117/12.595662.

[8] H. Lee, J. Lee, H. Kim, B. Cho, and S. Cho, "Deep-neural-network-based sinogram synthesis for sparse-view CT image reconstruction," *IEEE Trans. Radiat. Plasma Med. Sci.*, vol. 3, no. 2, pp. 109–119, Mar. 2019, doi: 10.1109/TRPMS.2018.2867611.

[9] M. Balda, J. Hornegger, and B. Heismann, "Ray contribution masks for structure adaptive sinogram filtering," *IEEE Trans. Med. Imag.*, vol. 31, no. 6, pp. 1228–1239, Jun. 2012, doi: 10.1109/TMI.2012.2187213.

[10] T. Li, X. Li, J. Wang, J. Wen, H. Lu, J. Hsieh, and Z. Liang, "Nonlinear sinogram smoothing for low-dose X-ray CT," *IEEE Trans. Nucl. Sci.*, vol. 51, no. 5, pp. 2505–2513, Oct. 2004, doi: 10.1109/TNS.2004.834824.

[11] A. Manduca, L. Yu, J. D. Trzasko, N. Khaylova, J. M. Kofler, C. M. McCollough, and J. G. Fletcher, "Projection space denoising with bilateral filtering and CT noise modeling for dose reduction in CT," *Med. Phys.*, vol. 36, no. 11, pp. 4911–4919, Oct. 2009, doi: 10.1118/1.3232004.

[12] J. Wang, T. Li, H. Lu, and Z. Liang, "Penalized weighted least-squares approach to sinogram noise reduction and image reconstruction for low-dose X-ray computed tomography," *IEEE Trans. Med. Imag.*, vol. 25, no. 10, pp. 1272–1283, Oct. 2006, doi: 10.1109/TMI.2006.882141.

[13] S. Kollem, "A fast computational technique based on a novel tangent sigmoid anisotropic diffusion function for image-denoising," *Soft Comput.*, vol. 28, nos. 11–12, pp. 7501–7526, Feb. 2024, doi: 10.1007/s00500-024-09628-9.

[14] H. Zhang, J. Ma, J. Wang, Y. Liu, H. Lu, and Z. Liang, "Statistical image reconstruction for low-dose CT using nonlocal means-based regularization," *Computerized Med. Imag. Graph.*, vol. 38, no. 6, pp. 423–435, Sep. 2014, doi: 10.1016/j.compmedimag.2014.05.002.

[15] Y. Chen, X. Yin, L. Shi, H. Shu, L. Luo, J.-L. Coatrieux, and C. Toumoulin, "Improving abdomen tumor low-dose CT images using a fast dictionary learning based processing," *Phys. Med. Biol.*, vol. 58, no. 16, pp. 5803–5820, Aug. 2013, doi: 10.1088/0031-9155/58/16/5803.

[16] J.-F. Cai, X. Jia, H. Gao, S. B. Jiang, Z. Shen, and H. Zhao, "Cine cone beam CT reconstruction using low-rank matrix factorization: Algorithm and a proof-of-principle study," *IEEE Trans. Med. Imag.*, vol. 33, no. 8, pp. 1581–1591, Aug. 2014, doi: 10.1109/TMI.2014.2319055.

[17] H. Zhang, J. Wang, D. Zeng, X. Tao, and J. Ma, "Regularization strategies in statistical image reconstruction of low-dose X-ray CT: A review," *Med. Phys.*, vol. 45, no. 10, pp. e886–e907, Sep. 2018, doi: 10.1002/mp.13123.

[18] S. Dong, P. Wang, and K. Abbas, "A survey on deep learning and its applications," *Comput. Sci. Rev.*, vol. 40, May 2021, Art. no. 100379, doi: 10.1016/j.cosrev.2021.100379.

[19] W. Yang, H. Zhang, J. Yang, J. Wu, X. Yin, Y. Chen, H. Shu, L. Luo, G. Coatrieux, Z. Gui, and Q. Feng, "Improving low-dose CT image using residual convolutional network," *IEEE Access*, vol. 5, pp. 24698–24705, 2017, doi: 10.1109/ACCESS.2017.2766438.

[20] Q. Xie, D. Zeng, Q. Zhao, D. Meng, Z. Xu, Z. Liang, and J. Ma, "Robust low-dose CT sinogram preprocessing via exploiting noise-generating mechanism," *IEEE Trans. Med. Imag.*, vol. 36, no. 12, pp. 2487–2498, Dec. 2017, doi: 10.1109/TMI.2017.2767290.

[21] D. Wu, K. Kim, G. E. Fakhri, and Q. Li, "Iterative low-dose CT reconstruction with priors trained by artificial neural network," *IEEE Trans. Med. Imag.*, vol. 36, no. 12, pp. 2479–2486, Dec. 2017, doi: 10.1109/TMI.2017.2753138.

[22] K. A. S. H. Kulathilake, N. A. Abdullah, A. Q. M. Sabri, and K. W. Lai, "A review on deep learning approaches for low-dose computed tomography restoration," *Complex Intell. Syst.*, vol. 9, no. 3, pp. 2713–2745, May 2021, doi: 10.1007/s40747-021-00405-x.

[23] W. Xia, H. Shan, G. Wang, and Y. Zhang, "Physics-/model-based and data-driven methods for low-dose computed tomography: A survey," *IEEE Signal Process. Mag.*, vol. 40, no. 2, pp. 89–100, Mar. 2023, doi: 10.1109/MSP.2022.3204407.

[24] C. You, L. Yang, Y. Zhang, and G. Wang, "Low-dose CT via deep CNN with skip connection and network in network," 2018, *arXiv:1811.10564*.

[25] M. Nishio, C. Nagashima, S. Hirabayashi, A. Ohnishi, K. Sasaki, T. Sagawa, M. Hamada, and T. Yamashita, "Convolutional auto-encoder for image denoising of ultra-low-dose CT," *Heliyon*, vol. 3, no. 8, Aug. 2017, Art. no. e00393, doi: 10.1016/j.heliyon.2017.e00393.

[26] F. Fan, H. Shan, M. K. Kalra, R. Singh, G. Qian, M. Getzin, Y. Teng, J. Hahn, and G. Wang, "Quadratic autoencoder (Q-AE) for low-dose CT denoising," *IEEE Trans. Med. Imag.*, vol. 39, no. 6, pp. 2035–2050, Jun. 2020, doi: 10.1109/TMI.2019.2963248.

[27] X. Dai, J. Bai, T. Liu, and L. Xie, "Limited-view cone-beam CT reconstruction based on an adversarial autoencoder network with joint loss," *IEEE Access*, vol. 7, pp. 7104–7116, 2019, doi: 10.1109/ACCESS.2018.2890135.

[28] M. P. Heinrich, M. Stille, and T. M. Buzug, "Residual U-net convolutional neural network architecture for low-dose CT denoising," *Current Directions Biomed. Eng.*, vol. 4, no. 1, pp. 297–300, Sep. 2018, doi: 10.1515/cdbme-2018-0072.

[29] J. Chi, C. Wu, X. Yu, P. Ji, and H. Chu, "Single low-dose CT image denoising using a generative adversarial network with modified U-net generator and multi-level discriminator," *IEEE Access*, vol. 8, pp. 133470–133487, 2020, doi: 10.1109/ACCESS.2020.3006512.

[30] H. Chen, Y. Zhang, M. K. Kalra, F. Lin, Y. Chen, P. Liao, J. Zhou, and G. Wang, "Low-dose CT with a residual encoder–decoder convolutional neural network," *IEEE Trans. Med. Imag.*, vol. 36, no. 12, pp. 2524–2535, Dec. 2017, doi: 10.1109/TMI.2017.2715284.

[31] C. K. Ahn, J. H. Kim, Z. Yang, C. Heo, H. Jin, and B. Park, "A deep learning-enabled iterative reconstruction of ultra-low-dose CT: Use of synthetic sinogram-based noise simulation technique," *Proc. SPIE*, vol. 10573, pp. 809–814, Mar. 2018, doi: 10.1117/12.2294013.

[32] Q. Ding, G. Chen, X. Zhang, Q. Huang, H. Ji, and H. Gao, "Low-dose CT with deep learning regularization via proximal forward–backward splitting," *Phys. Med. Biol.*, vol. 65, no. 12, Jun. 2020, Art. no. 125009, doi: 10.1088/1361-6560/ab831a.

[33] J. Adler and O. Öktem, "Learned primal-dual reconstruction," *IEEE Trans. Med. Imag.*, vol. 37, no. 6, pp. 1322–1332, Jun. 2018, doi: 10.1109/TMI.2018.2799231.

[34] J. He, Y. Yang, Y. Wang, D. Zeng, Z. Bian, H. Zhang, J. Sun, Z. Xu, and J. Ma, "Optimizing a parameterized plug-and-play ADMM for iterative low-dose CT reconstruction," *IEEE Trans. Med. Imag.*, vol. 38, no. 2, pp. 371–382, Feb. 2019, doi: 10.1109/TMI.2018.2865202.

[35] Q. Lyu, D. Ruan, J. M. Hoffman, R. Neph, M. McNitt-Gray, and K. Sheng, "Iterative reconstruction for low dose CT using plug-and-play alternating direction method of multipliers (ADMM) framework," *Proc. SPIE*, vol. 10949, pp. 36–44, Mar. 2019, doi: 10.1117/12.2512484.

[36] J. M. Wolterink, T. Leiner, M. A. Viergever, and I. Išgum, "Generative adversarial networks for noise reduction in low-dose CT," *IEEE Trans. Med. Imag.*, vol. 36, no. 12, pp. 2536–2545, Dec. 2017, doi: 10.1109/TMI.2017.2708987.

[37] J. Bai, X. Dai, Q. Wu, and L. Xie, "Limited-view CT reconstruction based on autoencoder-like generative adversarial networks with joint loss," in *Proc. 40th Annu. Int. Conf. IEEE Eng. Med. Biol. Soc. (EMBC)*, Honolulu, HI, USA, Jul. 2018, pp. 5570–5574, doi: 10.1109/EMBC.2018.8513659.

[38] X. Yin, Q. Zhao, J. Liu, W. Yang, J. Yang, G. Quan, Y. Chen, H. Shu, L. Luo, and J.-L. Coatrieux, "Domain progressive 3D residual convolution network to improve low-dose CT imaging," *IEEE Trans. Med. Imag.*, vol. 38, no. 12, pp. 2903–2913, Dec. 2019, doi: 10.1109/TMI.2019.2917258.

[39] Q. Ding, Y. Nan, H. Gao, and H. Ji, "Deep learning with adaptive hyper-parameters for low-dose CT image reconstruction," *IEEE Trans. Comput. Imag.*, vol. 7, pp. 648–660, 2021, doi: 10.1109/TCI.2021.3093003.

[40] H. Gupta, K. H. Jin, H. Q. Nguyen, M. T. McCann, and M. Unser, "CNN-based projected gradient descent for consistent CT image reconstruction," *IEEE Trans. Med. Imag.*, vol. 37, no. 6, pp. 1440–1453, Jun. 2018, doi: 10.1109/TMI.2018.2832656.

[41] G. T. Buzzard, S. H. Chan, S. Sreehari, and C. A. Bouman, "Plug-and-play unplugged: Optimization-free reconstruction using consensus equilibrium," *SIAM J. Imag. Sci.*, vol. 11, no. 3, pp. 2001–2020, Jan. 2018, doi: 10.1137/17m1122451.

[42] J. Wang, L. Zeng, C. Wang, and Y. Guo, "ADMM-based deep reconstruction for limited-angle CT," *Phys. Med. Biol.*, vol. 64, no. 11, May 2019, Art. no. 115011, doi: 10.1088/1361-6560/ab1aba.

[43] M. Akçakaya, B. Yaman, H. Chung, and J. C. Ye, "Unsupervised deep learning methods for biological image reconstruction and enhancement: An overview from a signal processing perspective," *IEEE Signal Process. Mag.*, vol. 39, no. 2, pp. 28–44, Mar. 2022, doi: 10.1109/MSP.2021.3119273.

[44] M. O. Unal, M. Ertas, and I. Yildirim, "An unsupervised reconstruction method for low-dose CT using deep generative regularization prior," *Biomed. Signal Process. Control*, vol. 75, May 2022, Art. no. 103598, doi: 10.1016/j.bspc.2022.103598.

[45] X. Jiang, M. Liu, F. Zhao, X. Liu, and H. Zhou, "A novel super-resolution CT image reconstruction via semi-supervised generative adversarial network," *Neural Comput. Appl.*, vol. 32, no. 18, pp. 14563–14578, May 2020, doi: 10.1007/s00521-020-04905-8.

[46] K. Liang, L. Zhang, H. Yang, Z. Chen, and Y. Xing, "A model-based unsupervised deep learning method for low-dose CT reconstruction," *IEEE Access*, vol. 8, pp. 159260–159273, 2020, doi: 10.1109/ACCESS.2020.3020406.

[47] M. Jiang and G. Wang, "Convergence of the simultaneous algebraic reconstruction technique (SART)," *IEEE Trans. Image Process.*, vol. 12, no. 8, pp. 957–961, Aug. 2003, doi: 10.1109/TIP.2003.815295.

[48] L. Calatroni, A. Lanza, M. Pragliola, and F. Sgallari, "Adaptive parameter selection for weighted-TV image reconstruction problems," *J. Phys., Conf. Ser.*, vol. 1476, no. 1, Mar. 2020, Art. no. 012003, doi: 10.1088/1742-6596/1476/1/012003.

[49] D. Ulyanov, A. Vedaldi, and V. Lempitsky, "Deep image prior," *Int. J. Comput. Vis.*, vol. 128, no. 7, pp. 1867–1888, Mar. 2020, doi: 10.1007/s11263-020-01303-4.
[50] A. Perelli and M. S. Andersen, "Regularization by denoising sub-sampled Newton method for spectral CT multi-material decomposition," *Phil. Trans. Roy. Soc. A, Math., Phys. Eng. Sci.*, vol. 379, no. 2200, May 2021, Art. no. 20200191, doi: 10.1098/rsta.2020.0191.
[51] M. Salehjahromi, Y. Zhang, and H. Yu, "Iterative spectral CT reconstruction based on low rank and average-image-incorporated BM3D," *Phys. Med. Biol.*, vol. 63, no. 15, Aug. 2018, Art. no. 155021, doi: 10.1088/1361-6560/aad356.
[52] M. Jian, X. Yu, H. Zhang, and C. Yang, "SwinCT: Feature enhancement based low-dose CT images denoising with swin transformer," *Multimedia Syst.*, vol. 30, no. 1, p. 1, Jan. 2024, doi: 10.1007/s00530-023-01202-x.
[53] D. O. Baguer, J. Leuschner, and M. Schmidt, "Computed tomography reconstruction using deep image prior and learned reconstruction methods," *Inverse Problems*, vol. 36, no. 9, Sep. 2020, Art. no. 094004, doi: 10.1088/1361-6420/aba415.
[54] X. Yi and P. Babyn, "Sharpness-aware low-dose CT denoising using conditional generative adversarial network," *J. Digit. Imag.*, vol. 31, no. 5, pp. 655–669, Feb. 2018, doi: 10.1007/s10278-018-0056-0.
[55] F. Wang, R. Wang, B. Yang, and H. Qiu, "Low-dose CT reconstruction using dataset-free learning," *PLoS ONE*, vol. 19, no. 6, Jan. 2024, Art. no. e0304738, doi: 10.2139/ssrn.4713174.
[56] M. O. Unal, M. Ertas, and I. Yildirim, "Proj2Proj: Self-supervised low-dose CT reconstruction," *PeerJ Comput. Sci.*, vol. 10, p. e1849, Feb. 2024, doi: 10.7717/peerj-cs.1849.

**RITU GOTHWAL** received the M.C.A. degree from Amity University, Manesar, India. She is currently pursuing the Ph.D. degree in computer science and engineering with the Thapar Institute of Engineering and Technology, Patiala, India. Her research interests include medical image reconstruction, image watermarking, and machine learning.

**SHAILENDRA TIWARI** received the Ph.D. degree in computer science and engineering from the Indian Institute of Technology (IIT) BHU, Varanasi. He is currently an Assistant Professor with the Department of Computer Science and Engineering, Thapar Institute of Engineering and Technology, Patiala. He was a Visiting Research Fellow (postdoctoral) with the School of Computer Science and Statistics (SCSS), Trinity College Dublin (TCD), Ireland. He has published more than 50 research articles in various reputed journals, conferences, and book chapters. His research interests include image processing, medical image reconstruction, and computer graphics and vision.

**SHIVENDRA SHIVANI** received the B.E. degree in computer science and engineering from CSVTU, in 2009, the master's degree in information security from the National Institute of Technology Allahabad, India, in 2011, and the Ph.D. degree in visual cryptography from the National Institute of Technology Allahabad. He is currently with the Thapar Institute of Engineering and Technology, Patiala, as an Assistent Professor. His current research interests include digital watermarking, pattern recognition, computer vision, algorithms, compression, biometrics, visual cryptography, and face recognition.